ingegneria sismica
International Journal of Earthquake Engineering
Anno XLIII - Num. 1 - 2026

Simulation of plastic deformation of materials during high-speed collisions and its computational analysis based on the finite element method

Jingtao Wang[1,2,*]

[1] CAEP Software Center for High Performance Numerical Simulation, Beijing, 100088, China
[2] Institute of Applied Physics and Computational Mathematics, Beijing, 100088, China

SUMMARY: *The degree of material deformation under extreme conditions is related to the safety of automobile driving. In this paper, the four-node Hughes-Liu unit (H4 unit), a shell unit commonly used in high-speed collision simulation of automobiles, is constructed, and the stress coordinates of each node are transferred to the overall coordinate system, which facilitates the calculation of the force at each place. Combined with the dynamics of the spring, the Lagrange method nonlinear finite element solution equations are applied to calculate the plastic deformation of the material of the car in the process of high-speed collision. According to the simulation test and finite element solution results, the materials of the three key structural points, namely B-pillar, A-pillar, and front longitudinal beam, show more serious deformation when subjected to high-speed collision, which cannot guarantee the integrity of the door frame and the safety of the occupants, and need to be optimized.*

KEYWORDS: *high-speed collision; H4 unit; coordinate transformation; nonlinear finite element; material plastic deformation*

1 Introduction

The design and manufacture of passenger cars, aerospace, ships, and long-distance pipelines have all raised the demand for evaluating the strong plastic intrinsic properties of materials under high strain rate conditions (1-103 s-) and even dynamic loading conditions [1, 2]. Especially for automotive steel, in order to meet the lightweight design of passenger cars need to “reduce weight, consumption and safety” requirements, the International Steel Association organized and initiated a new concept of ultra-lightweight steel frame body (ULSAB-AVC) project, is committed to the advanced high-strength automotive steel (AUSS) and supporting the research and development and promotion of manufacturing processes [3-5]. Among them, in the high-speed crash scenario, the stress-strain curves of materials under dynamic loading conditions as well as various types of strong and plastic performance indexes obtained through high-strain-rate tests are the key parameters for the subsequent design of the vehicle model and crash simulation calculation [6-8].

Under the high-speed collision behavior, the material is subjected to local melting and recrystallization phenomena due to the rate of temperature increase exceeding the rate of heat conduction and the interaction between grain boundaries and dislocations in metallic materials under high strain rate loading results in unorthodox static loading, which results in significant

---

[*] jtwang@126.com

https://doi.org/10.65102/is2026052

Published: 30 April, 2026

plastic deformation characteristics of the material, i.e., damage accumulation, mechanical differences in all directions, thermal effects, and strain rate sensitivity [9-13]. Generally, under static loading, irrecoverable macroscopic plastic deformation of the material occurs when the applied load reaches or exceeds the yield limit of the material [14]. In engineering applications, most of the mechanical component materials are subjected to dynamic loads rather than static loads during service. It is estimated that material damage due to dynamic loading may account for 50-90% of the total number of mechanical failures [15]. Impact load belongs to high strain rate loading dynamic load, the strength and plasticity of the material under the load will change, and its deformation and fracture mechanism can be completely different from static or quasi-static loading, and the form of failure and damage is also relatively special [16-18]. The cumulative plastic deformation will cause the size of the super difference and affect the normal use of parts and components, but also may lead to cracks and other defects, so that the failure of parts and components, bringing safety hazards and economic losses to the enterprise [19-21]. Therefore, the plastic deformation of materials under high-speed collision conditions has become a non-negligible failure factor of parts in engineering, and it is of great engineering significance to strengthen the research on plastic deformation of materials in high-speed collision.

Currently, the material response under high speed collision normal is carried out by numerical simulation methods, Finite Element Method (FEM), Discrete Element Method (DEM), and Smooth Particle Hydrodynamics (SPH). The DEM uses the dynamic relaxation method, Newton's second law, and time-stepping iterations to solve the motion and displacement of each particle, which is suitable for solving nonlinear problems. Liu et al [22] (2021) provided a DEM based on a Godunov-type continuous medium to simulate the dynamic response of the material under high velocity impacts, achieving accuracy in the description of discontinuities in the plastic characteristics of the material and the ability to multi-crack. Zhang and Liu [23] (2024) developed a viscous crack model using the DE-FE method to simulate the collision of complex agglomerates with the wall, which was combined with AFM measurements to determine the fragmentation pattern and plastic deformation. Habtemariam et al [24] (2025) established a DEM based method for simulation of vehicle-guard collision with the help of a small number of 3D non-spherical particles to describe the vehicle and the guard, which reduces the computational time and makes the calculation more accurate and complete. Nguyen et al [25] (2021) integrated DEM and viscoplastic beam model for 3D simulation of elastic-plastic deformation of ductile materials, and experimental tests verified the strong potential of FEM for fracture, large deformation, and elastic-plastic simulation of brittle materials.

SPH describes continuous fluids in a unique discrete ionic form and approximates the fluid dynamics equations through a series of complex computational processes suitable for solving extreme deformation and fracture problems. Chaussonnet et al [26] (2020) used SPH to simulate the behavior of high-speed collisions of molten sand particles against the solid wall of a gas turbine and found that the particles do not appear to be flaky as a result of the impact, but the normal pressure increases in the normal direction. Frissane et al [27] (2019) simulated the penetration process of a blunt projectile impacting a thin metal plate with the help of 3D SPH and meshless particle analysis, and introduced an elastic-plastic model and a simplified damage model to simulate the mechanical behavior therein, which clarified the material deformation, damage, and rupture of the penetration phenomenon that occurs at high speed impact. Wang et al [28] (2025) simulated the high-velocity impact performance of spacecraft composite shielding structures by coupling SPH and FEM to incorporate debris cloud spreading and projectile energy profiles to evaluate the impact performance, and the computational efficiency of this coupled approach was greatly increased.

The FE method discretizes the overall structure into a finite number of small cells, performs finite element calculations on each small cell, and obtains the overall results through integration, which is suitable for solid structure analysis and has high flexibility in meshing and convenient condition processing, which makes it have a strong potential for high-speed collision simulation. Cerik [29] (2017) applied nonlinear FEM to simulate the large inelastic deformation of aluminum alloy plates of marine-grade ships under high-speed impact, simplified the impact pressure curve, set boundary conditions, and successfully described the large deformation state of the aluminum alloy plates. Xie et al [30] (2018) simplified the single-vehicle model and the overall FEM model of the unplasticized portion of the collision simulation of multiple high-speed trains, which allowed the computational efficiency and computational correctness of the model to be improved in the simulation. Han et al [31] (2018) used FEM software to simulate the behavior of wheel-track collisions triggered by wheel rupture in high-speed trains, and found that the strain effect of such collisions is significant on the equivalent plastic strain, which is sensitive to train speed and wheel properties. Zhang et al [32] (2021) constructed a high-precision FEM model for a small rotary-wing logistics UAV to simulate the UAV collision behavior, which clearly presented the collision damage process and components, as well as the collision failure mode. Kota et al [33] (2020) created a FEM model of light fixed-wing unmanned aerial vehicle (UAV) components, which was able to effectively simulate the nonlinear characteristics of material changes in airborne collisions for both unmanned and manned aircraft. DeLeon and alazotto et al [34] (2020) simulated microconvex body collisions at hypersonic velocities with a FEM model, which was used to understand the damage changes in the microstructure of the boot and track material under extreme environments due to collisions. Komine et al [35] (2023) designed a high-speed particle collision experimental method for obtaining plastically deformed material parameters at high strain rates, introduced FEM to simulate the deformation behavior, and determined the intrinsic equations of plastic deformation of the material from a microscopic point of view.

This paper takes an automobile as an example, focuses on the plastic deformation of materials during high-speed collision, and researches the structure and position of materials that need to be adjusted through the method of simulation test and finite element solution. The H4 unit is applied to restore the information of material material and force at each key structural point, and this information is clearly converted to the overall coordinate system, which is convenient to visualize the material change process of the car during high-speed collision. The dynamics of spring is introduced to measure the energy change of automobile materials during the collision process. Finally, the nonlinear finite element method described by Lagrange's method is applied to solve the energy conservation, displacement change, and shape change of each key structural point, and to simulate and calculate the plastic deformation of the material during high-speed collision.

2 High-speed crash simulation methods combined with finite element analysis

2.1 H4 cell in automobile high-speed crash simulation

Most of the structural components of automobiles are made of thin shells and plates, so the most commonly used unit in automobile crashworthiness analysis is the three-dimensional thin-shell unit, and only a small number of beam units and body units are used. The following is a brief introduction to the four-node Hughes-Liu unit (H4 unit for short), which is a shell unit commonly used in automotive high-speed crash simulation.

The Hughes-Liu thin shell unit is a four-node quadrilateral thin shell unit degraded from an 8-node six-sided solid unit. It is suitable for large displacements, large rotations and large strains. It satisfies the two basic assumptions of the thin-shell unit:

1) The line strain perpendicular to the center plane can be neglected;

2) Normal stresses on the cross section parallel to the midplane can be neglected.

The natural coordinates of the shell cell are ($\hat{\imath}$, ç, æ). æ-invariant surfaces are called dimensions, and $\hat{\imath}$ and ç-invariant lines are called fibers (along the shell thickness direction).

When an 8-node hexahedral solid unit degenerates into a 4-node quadrilateral shell unit, each shell unit node corresponds to a node of the 2 solid units, connected by a non-elongated fiber. This constraint degrades the 6 degrees of freedom of the 2 nodes of the solid cell into 5 degrees of freedom of the 1 node of the shell cell. Although the length of this fiber is kept constant during time-step calculations, the program can modify the shell cell thickness after each time-step calculation by straining the nodes along the thickness direction.

To facilitate the definition of contact interfaces or the calculation of reinforced shells, the level at which the Hughes-Liu thin shell unit nodes are located (called the reference surface) $\zeta = \bar{\zeta}$ can be chosen in three ways: $\bar{\zeta} = 0.0$ nodes are located at the mid-surface of the shell unit; $\bar{\zeta} = 1.0$ nodes are located at the top-surface of the shell unit; and $\bar{\zeta} = -1.0$ node is located at the bottom face of the shell unit.

The stress state of the thin-shell unit is the plane stress state within the level, and the positive stress between the levels of the unit must be equal to zero in the intrinsic relationship operation, but the stored data is the stress value under the overall coordinate system, for this reason, it is necessary to establish the conversion relationship between the local coordinate system of the thin-shell unit level and the overall coordinate system. The base vector used for the local coordinate system at the thin-shell unit level is $\left(\vec{e}_1, \vec{e}_2, \vec{e}_3\right)$, where $\vec{e}_3$ is the normal unit vector perpendicular to the thin-shell unit level, and the equation is:

$$\vec{e}_3 = \left(\vec{l}_\xi \times \vec{l}_\eta\right) \Big/ \left\|\vec{l}_\xi \times \vec{l}_\eta\right\| \tag{1}$$

Among them, $\vec{l}_\xi, \vec{l}_\eta$ are vectors parallel to the directions of $\hat{\imath}$ and ς respectively.

The base vectors and shell units of $\vec{e}_1$ and $\vec{e}_2$ When the levels are tangent, the formula is

$$\vec{e}_1 = \vec{l}_\xi \Big/ \left\|\vec{l}_\xi\right\| \tag{2}$$

$$\vec{e}_2 = \vec{e}_3 \times \vec{e}_1 \tag{3}$$

The transformation of the level local coordinate system vector $\hat{\vec{L}}$ to the overall coordinate system vector $\vec{L}$ is:

$$\hat{\vec{L}} = e\left[\vec{e}_1 \;\; \vec{e}_2 \;\; \vec{e}_3\right]\vec{L} \text{ Or } \hat{\vec{L}} = [q]\vec{L} \tag{4}$$

When numerical integration is used to calculate the unit stress scatter $\int_{v_m} \left[B\right]^T \left\{\sigma\right\} dv$, a single point of integration is used within the layer level (æ is constant) (the center of the layer level is the location of the integration point) but in the direction of the thickness of the shell element, the user has a various options, i.e., Gaussian integration (2-5 integration points), trapezoidal rule (equally spaced integration points with unlimited number of points), and user-defined integration rule, to facilitate the calculation of composite laminated shells and sandwich shells.

In order to ensure that the value of normal stress perpendicular to the level is zero, i.e., $\sigma_{33} = 0.0$, the stress at the unit integration point should be corrected in the local coordinate system along the lines described below.

Considering that there is a large rotation in the large deformation of the structure, the stress rate (derivative of stress to time) corresponding to the strain rate in the constitutive equation must be an objective tensor with invariance about the rotation of the rigid body, and the Jaumann stress rate $\overset{\triangledown}{\sigma}_{ij}$ just meets this condition, if the stress correction is made by using the Jaumann stress rate, the At this time the time derivative of the Cauchy stress is expressed as:

$$\dot{\sigma}_{ij} = \overset{\triangledown}{\sigma}_{ij} + \sigma_{ik}\Omega_{kj} + \sigma_{jk}\Omega_{ki} \tag{5}$$

where Ω_{ij} is the rotation tensor:

$$\Omega_{ij} = \frac{1}{2}\left(\frac{\partial \dot{x}_j}{\partial x_i} - \frac{\partial \dot{x}_i}{\partial x_j}\right) \tag{6}$$

Before the stress correction, the stress at the t_n moment σ_{ij}^n is updated to the stress of the configuration at the t_{n+1} moment:

$$\sigma_{ij}^{n+1} = \sigma_{ij}^{n} + \left(\sigma_{ip}^{n}\Omega_{pj}^{n+\frac{1}{2}} + \sigma_{jp}^{n}\Omega_{pi}^{n+\frac{1}{2}}\right)\Delta t_{n+\frac{1}{2}} \tag{7}$$

Transforming the stress and strain rates of the above equation in the general coordinate system to the local coordinate system of shell elements at the moment of t_{n+1}, we have:

$$\hat{\underline{\sigma}}_{ij}^{n+1} = R_{ik}R_{jl}\sigma_{kl}^{n+1} \tag{8}$$

$$\hat{\varepsilon}_{ij}^{n+\frac{1}{2}} = R_{ik}R_{jl}\varepsilon_{kl}^{n+\frac{1}{2}} \tag{9}$$

where R_{ij} is the orthogonal transformation matrix between the general and local coordinate systems.

The stress correction in the local coordinate system is:

$$\hat{\underline{\sigma}}_{ij}^{n+1} = \hat{\dot{\underline{\sigma}}}_{ij}^{n+1} + C_{ijkl}\hat{\varepsilon}_{kl}^{n+\frac{1}{2}}\Delta t_{n+\frac{1}{2}} \tag{10}$$

where C_{ijkl} is the planar stress eigenstructure matrix in the local coordinate system, and then the stress tensor is transformed to the general coordinate system with:

$$\sigma_{ij}^{n+1} = R_{ki} R_{lj} \hat{\sigma}_{kl}^{n+1} \tag{11}$$

The value of the cell stress dispersion is then calculated by numerical integration.

2.2 Dynamics of the simulation model

In general, a typical spring is elasto-plastic. This means that it has at least two different values of spring stiffness (one for the loaded case and the other for the unloaded case). Figure 1 shows the force-deflection characteristics of an elasto-plastic spring. d_c is the dynamic collision deflection; d_p is the permanent deflection; d_e is the elastic rebound displacement, $d_e = d_c - d_p$; F_1 is the force at d_c; k_L is the loading stiffness; and k_U is the unloading stiffness.

Figure 1 shows a special case of the spring deformation process, i.e. its permanent deformation is obtained (intercept d_p of the unloaded diagonal k_U on the horizontal axis of the zero force). Classification of springs into the following 3 types depends on the value of the unloading stiffness:

1) Elastic: $k_U = k_L$, there is no energy loss and the spring returns to its initial position;

2) plastic: $k_U = \infty$, all the absorbed energy is consumed, there is no rebound and the maximum deflection occurs at the permanent deformation, $d_c = d_p$;

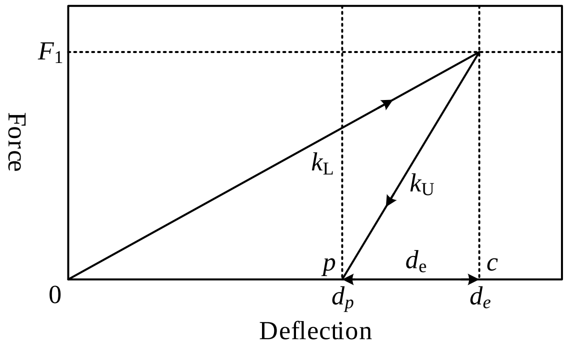

Figure 1: Force defleclion characteristics of elastoplastic spring

3) Elastic-plastic: $k_U > k_L$, the energy consumed is equal to the area of the triangle in Fig. 1, the area under the force-deflection curve in the loaded state minus the area under the force-deflection curve in the unloaded state, and the spring rebounds to reach permanent deformation.

If $k_U < k_L$, there is no rebound, i.e., the spring remains in the loaded state.

The following relationship is established to define the independence between the linear loading stiffness k_L and the linear unloading stiffness:

Maximum spring force at d_c:

$$F_1 = k_L d_c = k_U d_e \tag{12}$$

$$\frac{d_e}{d_c} = \frac{k_L}{k_U} \tag{13}$$

The collision energy is absorbed at d_c :

$$\Delta E = \frac{1}{2} k_L d_c^2 = \frac{1}{2} m v^2 \tag{14}$$

Rebound Energy:

$$\Delta E' = \frac{1}{2} k_U d_e^2 = \frac{1}{2} m v'^2 \tag{15}$$

$$\frac{\Delta E'}{\Delta E} = \left(\frac{v'}{v}\right) = e^2 \tag{16}$$

Energy Consumption:

$$\Delta E_d = \Delta E - \Delta E' = \Delta E \left(1 - e^2\right) \tag{17}$$

$$\frac{\Delta E'}{\Delta E} = \frac{k_U d_e^2}{k_L d_c^2} \tag{18}$$

where: ΔE is the total collision energy absorbed at d_c ; $\Delta E'$ is the recovered elastic energy; v is the vehicle collision velocity; v' is the vehicle rebound velocity; and e is the coefficient of recovery (COR).

Substituting equations (13) and (16) into Eq. (18), we get

$$e^2 = \frac{k_L}{k_U} \tag{19}$$

$$k_U = \frac{k_L}{e^2} \tag{20}$$

$$e = \sqrt{\frac{d_e}{d_c}} \tag{21}$$

It can be seen that the linear spring stiffness ratio for the 2 (loaded and unloaded) different models is equal to the square of the recovery coefficient e. The coefficient of recovery e is equal to $0\left(k_U = \infty\right)$ for fully plastic collisions and $1\left(k_U = k_L\right)$ for fully elastic collisions.

2.3 Nonlinear finite element solution equations

At present, Lagrange method is the most mature and convenient method to describe the solid collision behavior. The finite element method described by Lagrange method can deal with complex boundary conditions and complex material constitutive relations in high-speed collision engineering, and it is very convenient to describe the contact slip surface, and the main algorithm of LS-DYNA, which is the most widely used in the computer simulation of automobile collision, adopts the Lagrange method.Lagrange method describes the equilibrium equations of the basic equations and structural discretization, and its basic equations mainly include the mass conservation and energy conservation equations of continuous medium mechanics. Lagrange method describes the basic equations and structural discrete equilibrium equations, and its basic equations mainly include the mass conservation, momentum conservation, energy conservation equations of the mechanics of the continuous medium.

1) Description of the configuration of the object and the equation of conservation of mass

Figure 2 shows the process of object motion. In the Cartesian coordinate system of Fig. 2, B is the initial configuration of the object, and after a certain time t, its present configuration is b. Any point $X_a\left(a=1,2,3\right)$ in B becomes the point $x_i\left(i=1,2,3\right)$ in the present configuration after time t. In continuum mechanics, where objects and their deformations and motions are assumed to be continuous, it is shown that each point X_a in B corresponds to and only to one prime point x_i in b and vice versa. Using the Lagrange description method, the present configuration is expressed in terms of the initial configuration:

$$x_i = x_i\left(X_a, t\right)\left(i=1,2,3\right) \tag{22}$$

Let $t=0$, the initial condition can be found as

$$x_i\left(X_a, 0\right) = X_a \tag{23}$$

$$\dot{x}\left(X_a, 0\right) = V_a \tag{24}$$

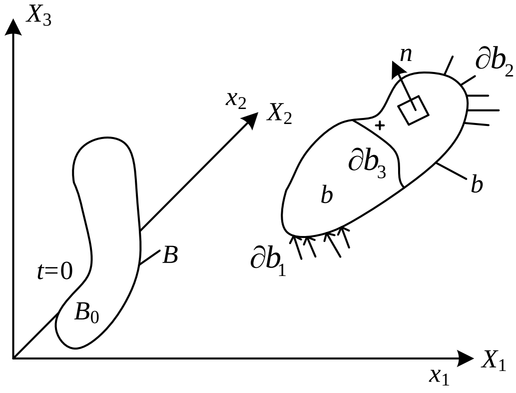

Figure 2: The illustration of body movement

Conservation of mass can be expressed as:

$$\rho = J\rho_0 \tag{25}$$

where ρ is the current mass density, ρ_0 is the initial mass density, and J is the relative volume coefficient, i.e., the determinant value of the Jacobi matrix $F_{ij} = \dfrac{\partial x_i}{\partial X_j}$.

2) Differential equations of motion

If any closed surface S is taken on an object, the volume V enclosed within the S surface. If the physical force (e.g., gravity, etc.) on a unit volume of the medium within V is $\rho f_i dv$, where ρ is the density of the medium and f_i is the external force on a unit mass of the medium, then the total physical force on the medium within V is $\int_V \rho f_i dv$. In addition to the body force, the medium inside the closed surface will also be subjected to the surface force. Let a face element ds be selected at any point on the closed face, and if the total stress component on ds is σ_{ni}, the force on the ds face is $\oint \sigma_{ni} \bullet ds$. Therefore, the combined force on the medium inside the closed surface is $\oint \sigma_{ni} \bullet ds + \int_V \rho f_i dv$. If the relative displacements between points within the medium are neglected (under the small deformation assumption) and μ_i denotes the displacement vector at a point within the S-plane, we have, according to Newton's second law:

$$\oint \sigma_{ni} \bullet ds + \int_V \rho f_i dv = \int_V \rho \frac{\partial^2 \mu_i}{\partial t^2} dv \tag{26}$$

Substituting $\sigma_{ni} = \sigma_{ji} n_j$, we get

$$\oint \sigma_{ji} n_j ds + \int_V \rho f_i dv = \int_V \rho \frac{\partial^2 \mu_i}{\partial t^2} dv \tag{27}$$

Using Gauss's theorem, we can obtain

$$\oint A_i n_i ds = \oint \frac{\partial A_i}{\partial x_i} dv \tag{28}$$

The above equation can be reduced to

$$\int_V \left(\frac{\partial \sigma_{ji}}{\partial x_j} + \rho f_i \right) dv = \int_V \rho \frac{\partial^2 \mu_i}{\partial t^2} dv \tag{29}$$

Since the S-plane is arbitrarily taken, it can be made to contract to a point, where there is

$$\frac{\partial \sigma_{ji}}{\partial x_j} + \rho f_i = \rho \frac{\partial^2 \mu_i}{\partial t^2} \tag{30}$$

This equation is the differential representation of the equation of motion under discussion, referred to as the differential equation of motion, which reveals the relationship between force and acceleration at a point within an object.

Corresponding to different boundaries are satisfied respectively:

a) The traction boundary condition is satisfied at the boundary ∂b_1:

$$\sigma_{ij} n_j = t_i(t) \tag{31}$$

b) The displacement boundary condition is satisfied at the boundary ∂b_2:

$$x_i\left(X_a, t\right) = D_i\left(t\right) \tag{32}$$

c) The contact continuity condition is satisfied on the interior boundary ∂b_3 when $x_i^+ = x_i^-$:

$$\left(\sigma_{ij}^+ - \sigma_{ij}^-\right) n_i = 0 \tag{33}$$

In the above equations, σ_{ij} is the Cauchy stress tensor, n_i is the normal unit vector outside the boundary ∂b, $t_i\left(i = 1,2,3\right)$ is the surface force loading, and $D_i\left(i = 1,2,3\right)$ is the given displacement function.

3) Energy equation

$$\dot{E} = VS_{ij}\dot{\varepsilon}_{ij} - \left(p+q\right)\dot{V} \tag{34}$$

where, V - volume of the present configuration;

$\dot{\varepsilon}_{ij}$ - strain rate tensor;

q - volumetric viscous resistance;

Partial stress tensor - $S_{ij} = \sigma_{ij} + (p+q)\delta_{ij}$;

Hydrostatic pressure - $P = -\frac{1}{3}\delta_{ij} - q = -\frac{1}{3}\sigma_{kk} - q$, $\delta_{ij} = \begin{cases} 1 & i = j \\ 0 & i \neq j \end{cases}$.

The Galyokin method of weak equilibrium can be written:

$$\begin{aligned} &\int_V \left(\rho\ddot{x}_{ij} - \sigma_{ij,j} - \rho f_i\right)\delta x_i dv + \int_{\partial b_3} \left(\sigma_{ij}^+ - \sigma_{ij}^-\right) n_j \delta x_i ds \\ &+ \int_{\partial b_1} \left(\sigma_{ij} n_j - t_i\right)\delta x_i ds = 0 \end{aligned} \tag{35}$$

where δx_i satisfies all displacement boundary conditions on the ∂b_2 boundary.

Applying the scattering theorem to the above equation has:

$$\int_V \left(\sigma_{ij}\delta x_{i,j}\right) dv = \int_{\partial b_1} \sigma_{ij} n_j \delta x_i ds + \int_{\partial b_3} \left(\sigma_{ij}^+ - \sigma_{ij}^-\right) n_j \delta x_i ds \tag{36}$$

And step-by-step points for:

$$\left(\sigma_{ij}\delta x_{i,j}\right) - \sigma_{ij,j}\delta x_i = \sigma_{ij}\delta x_{i,j} \tag{37}$$

So the above equation can be rewritten as a variation of the virtual work principle into a disaggregated equation:

$$\delta\pi = \int_V \rho\ddot{x}_i \delta x_i dv + \int_V \sigma_{ij}\delta x_{i,j} dv - \int_V \rho f_i \delta x_i dv - \int_{\partial b_1} t_i \delta x_i ds \tag{38}$$

4) Structural finite element discretization

If a finite element discretization of the object is performed, the coordinates of any point within the cell are expressed by coordinate node interpolation as:

$$x_i\left(X_a,t\right)=x\left(X_a\left(\xi,\zeta,\eta\right),t\right)=\sum_{j=1}^{k}\phi_j\left(\xi,\zeta,\eta\right)x_i^j(t) \tag{39}$$

where ϕ_j is the form function expressed in parametric coordinates $\left(\xi,\zeta,\eta\right)$, k is the number of cell nodes, and x_i^j denotes the displacement of the jth node of the cell in the $i\left(i=1,2,3\right)$ direction.

Summing the imaginary work of the n cells of the whole object, there are:

$$\delta\pi=\sum_{m=1}^{n}\delta\pi_m=0 \tag{40}$$

To wit:

$$\sum_{m=1}^{n}\left\{\int_{v_m}\rho x\phi_i^m dv+\int_{v_m}\sigma_{ij}^m\phi_{i,j}^m dv-\int_{v_m}\rho f_i\phi_i^m dv-\int_{\partial b_1}t_i\phi_i^m ds\right\} \tag{41}$$

Among them:

$$\phi_i^m=\left(\phi_1,\phi_2,\ldots,\phi_k\right)_i^m \tag{42}$$

Write the above equation in matrix form:

$$\begin{aligned}&\sum_{m=1}^{n}\left\{\int_{v_m}\rho[N]^r[N]\{\ddot{x}\}^c dv+\int_{v_m}[B]^T\{\sigma\}dv\right.\\&\left.-\int_{v_m}\rho[N]^T\{b\}dv-\int_{ab_1}[N]^T\{t\}ds\right\}^m=0\end{aligned} \tag{43}$$

where $\left[N\right]$ is the shape function matrix, $\left\{\sigma\right\}$ is the Cauchy stress vector, and

$$\{\sigma\}^T=\left(\sigma_{xx},\sigma_{yy},\sigma_{zz},\sigma_{xy},\sigma_{yz},\sigma_{zx}\right) \tag{44}$$

$$\begin{Bmatrix}\ddot{x}_1\\\ddot{x}_2\\\ddot{x}_3\end{Bmatrix}=\begin{Bmatrix}\ddot{x}_1^1\\\ddot{x}_2^1\\\vdots\\\ddot{x}_3^k\end{Bmatrix}=[N]\{\ddot{x}\}^e \tag{45}$$

where: $\left\{b\right\}$ is the volume force vector

$\left\{t\right\}$ is the traction force vector, and

$$\{b\}=\begin{Bmatrix} f_1 \\ f_2 \\ f_3 \end{Bmatrix},\{t\}=\begin{Bmatrix} t_1 \\ t_2 \\ t_3 \end{Bmatrix} \tag{46}$$

The unit calculations of the above equations are combined to obtain the discretized system equilibrium equations:

$$[M]\{\ddot{x}(t)\}=\{P(x,t)\}-\{F(x,\dot{x})\} \tag{47}$$

where $[M]$ is the overall diagonal mass matrix after grouping, $\{\ddot{x}(t)\}$ is the overall nodal acceleration vector, $\{P\}$ is the total nodal load vector, and $\{F\}$ is the equivalent nodal vector grouping of the unit stress field:

$$\{F\}=\sum_{m=1}^{n}\int_{v_m}[B]^T\{\sigma\}dv \tag{48}$$

The above equation is solved by applying the display center difference method.

3 High-speed crash test and finite element calculation practice

3.1 High-speed crash simulation test credibility analysis

3.1.1 Energy changes in whole-vehicle high-speed crashes

In order to judge that the simulated high-speed collision process can accurately reflect the plastic deformation of automobile materials and to improve the accuracy of the nonlinear finite element solution, a high-speed collision test of an automobile is set up. The reliability of the simulation results is analyzed in terms of the energy conservation and local velocity changes in the high-speed collision of the whole car. Figure 3 shows the energy change curve in the whole car collision. The initial speed of the whole car collision is set to 50km/h, the gravitational acceleration is 9.8m/s^2, and the collision time is set to 0.3 s. In Fig. 3, it can be seen that the total energy curve is basically maintained in a horizontal state during the collision process (8.99*10^{8}J), which is close to a straight line, which indicates that the law of energy conservation is observed in the collision. The kinetic energy curve starts to decline rapidly when the car touches the rigid wall, and falls to the lowest value at about 0.142s, after which the curve rises slightly, when the car bounces back at a low speed. The internal energy curve and the kinetic energy curve are in mirror relationship, which indicates that the kinetic energy is transformed to the internal energy in the collision stage of the car, and the maximum value of the absorbed energy is 8.31*10^{8}J, which accounts for 92.44% of the total energy, so it can be seen that the body structure absorbs a great deal of the collision energy in the collision. The hourglass energy change curve is always at a very low level during the collision. About 5.95% of the total energy. The simulation effect of the whole vehicle energy change is in line with the actual high-speed collision process.

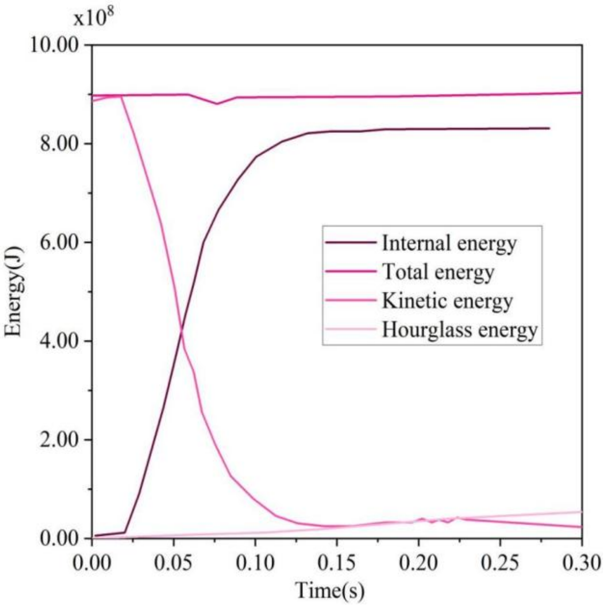

Figure 3: Energy change curve in vehicle collision

3.1.2 Acceleration comparisons for localized high-speed collisions

According to the results of the existing test data, acceleration sensors are set up at the top and bottom of the engine and the center channel of the vehicle in the finite element model of the whole vehicle to output the acceleration at the bottom and top of the engine and the center channel, respectively, for comparison with the test data. Figure 4 shows the comparison results of local position acceleration. From the comparison of data curves in Fig. 4, it can be seen that there are some differences between the simulation model test data and the real vehicle test data in the size of the acceleration at the three positions, but the time of the first appearance of the peak value (0.049s, 0.056s, 0.018s) is almost the same between the simulation test results and the real vehicle test results, and the two curves are roughly the same in terms of the overall trend, which illustrates that the simulation test model The simulation test results are almost the same as the real vehicle test results, and the two curves are also approximately the same in the overall trend, indicating that the simulation test model is basically consistent with the real vehicle test results.

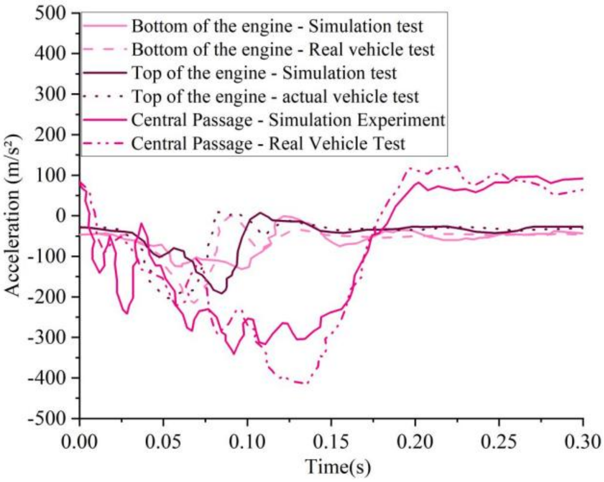

Figure 4: Comparison results of local position acceleration

3.2 Plastic deformation of materials in high-speed collisions

3.2.1 Analysis of B-column acceleration change

After testing the credibility of the deformation of the model simulating a high-speed collision through tests, the whole vehicle crash simulation and safety analysis formally begins. Among them, it is very important to monitor the acceleration of key structural points, which is helpful to evaluate and calculate the behavior of the vehicle in a high-speed collision event as well as the impact force that the occupants may suffer. The B-pillar structural point near the occupants, the front longitudinal beam, and the A-pillar are taken as the key structural points to be monitored, and the corresponding measurement points are set up at these locations near the door frame to capture the dynamic response during the collision. Figure 5 shows the B-pillar acceleration curve. During the high-speed collision, the maximum acceleration at the B-pillar location reaches 44.95g, and the minimum acceleration is -10.50g.

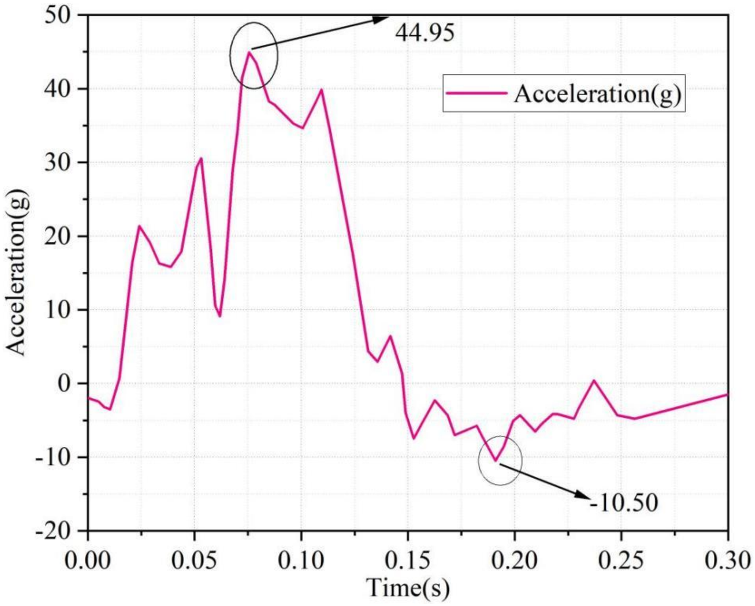

Figure 5: B-pillar acceleration curve

3.2.2 Front longitudinal beam displacement and deformation analysis

The material design and structural strength of the front longitudinal beam directly affect the efficiency of crash energy absorption and the degree of protection of the occupant compartment. By accurately calculating and evaluating the displacement change of the front longitudinal beam relative to the rest of the body, important information about the overall collapse of the front longitudinal beam can be obtained. Figure 6 shows the displacement of the front longitudinal beam during a high-speed crash. From the figure, it can be seen that the overall displacement of the front longitudinal beam is 135.41 mm.

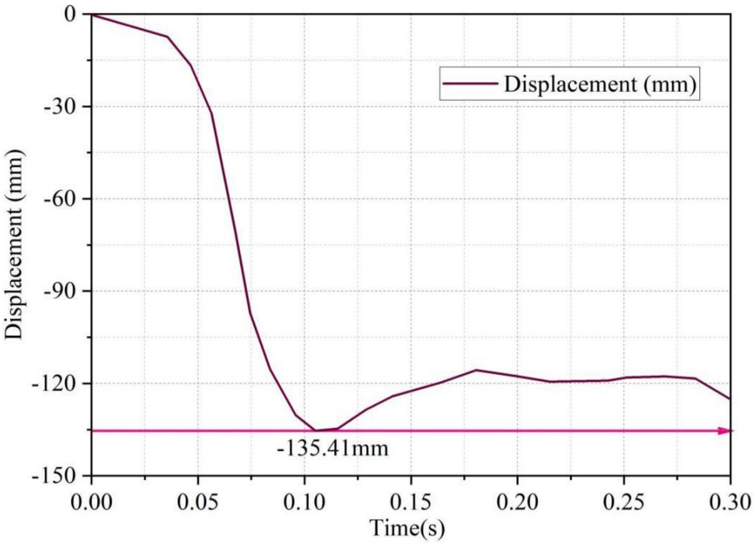

Figure 6: The displacement of the front longitudinal beam

3.2.3 A-pillar bending analysis

In high-speed crash simulation, the amount of deformation of the A-pillar is one of the indicators of the integrity of the passenger compartment and the safety of the passengers.The A-pillar not only supports the windshield of the vehicle, but also endures a great impact force in a frontal collision.The bending and intrusive deformation of the A-pillar directly affect the space of the passenger compartment, which may increase the risk of injury to the driver in a collision. In order to evaluate the degree of deformation of the A-pillar in a collision, three key points are selected: A, O, and B. The angle change of ∠AOB is used to observe whether the A-pillar bends during the collision. Figure 7 shows the change of angle of A-pillar. In the collision process, the A-pillar was bent from 0° to 9.08°, and the bending was more serious. This indicates that the front-end structure of the vehicle needs to be optimized for energy absorption and dispersion.

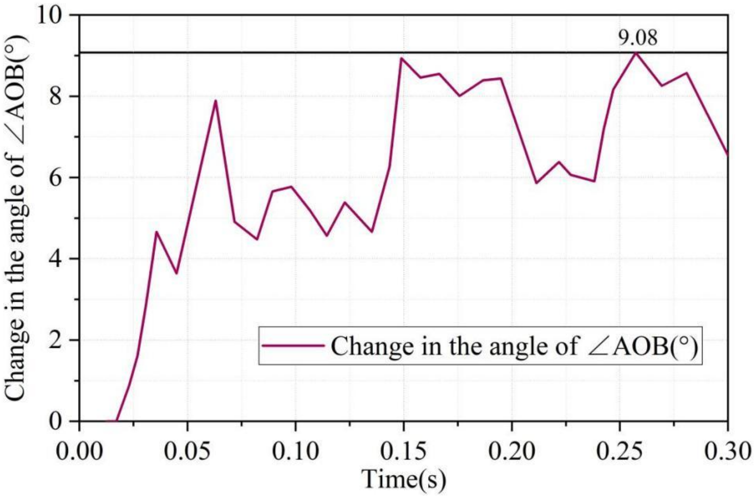

Figure 7: Change in the angle of the A-pillar

3.3 Nonlinear finite element solution results

3.3.1 Displacement variation of the aft node of the front longitudinal girder

Through the high-speed crash simulation test, it is possible to visualize the basic changes such as displacements at the three key structural points. To understand the material deformation therein in detail, it is necessary to combine the nonlinear finite element solution equations to solve them one by one. For the front longitudinal beam, the material at its head and tail position is more prone to collapse and downward bending, which requires special attention. Figure 8 shows the X-direction displacement change of a node at the end of the front longitudinal beam obtained by nonlinear finite element solution. The displacement of this node at the aft end of the front longitudinal beam changes rapidly to 120.96 mm at 0.104 s, after which the displacement reaches a maximum of 125.66 mm at 0.131s. The end of the front longitudinal beam material has undergone very serious downward bending deformation, which results in the weak bearing capacity of the front longitudinal beam, which is unable to fully absorb the collision force, and cannot ensure the integrity of the passenger compartment, which may jeopardize the safety of the occupants' lives. Therefore, it is necessary to reinforce the front longitudinal beam and select more stable and impact-resistant materials to reduce the risk of deformation of the front longitudinal beam.

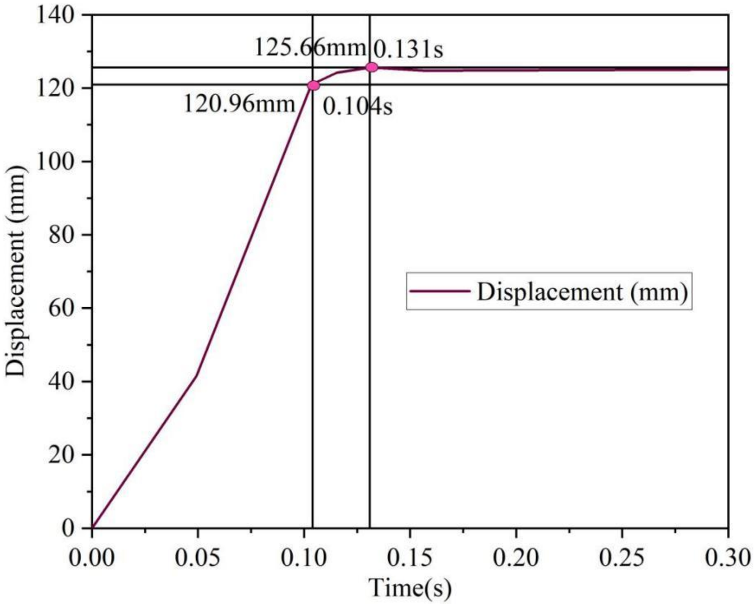

Figure 8: X-direction displacement of rear end node of front longitudinal beam

3.3.2 Analysis of door frame intrusions

The position of B-pillar is near the door frame, which can better reflect the deformation of the door frame under high-speed collision. Two points are taken as reference points at the corresponding positions of the B-pillar, and two points are taken as measurement points at the upper and lower hinges of the door frame, and the deformation of the door frame is analyzed by solving the displacement change in the X-direction of the measurement points with respect to the reference points through the nonlinear finite element. Figure 9 shows the time-dependent deformation of the door frame on the collision side at the measurement points. After the collision, the deformation of both measurement points starts to increase, and at the end of the collision, the final deformation is calculated to be 24.91 mm and 20.19 mm. According to the safety regulations, the deformation of the upper and lower hinges should not be more than 20 mm, so as to ensure that the occupants can open the door normally after the end of the collision. Combined with the B-pillar reference point and the nonlinear finite element solution, it is found that the deformation at the upper and lower hinges of the door frame exceeds the safety regulations, and the plastic deformation of the material is more serious, which needs to be optimized in the following.

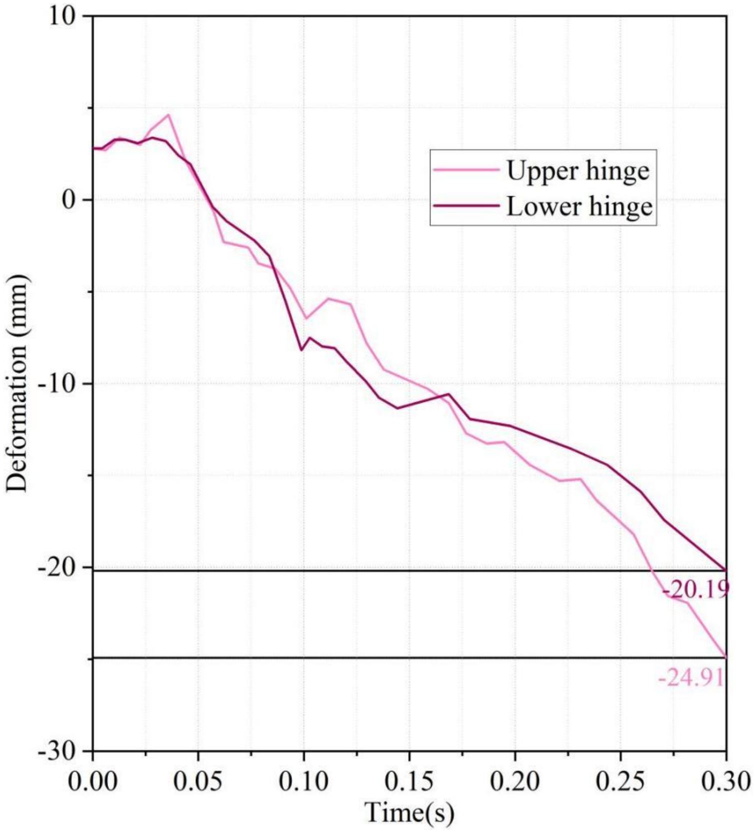

Figure 9: Deformation of the side door frame over time due to collision

3.3.3 Intrusion of column A relative to column B

In a vehicle collision, the degree of deformation of the A-pillar not only directly affects the structural integrity of the passenger compartment, but also its intrusion relative to the B-pillar is one of the key indicators for evaluating the safety of the occupants, and this parameter directly determines the degree of deformation of the door frame, which in turn affects the openability of the door. Figure 10 shows the intrusion amount of A-pillar relative to B-pillar obtained by nonlinear finite element solution. The maximum intrusion of A-pillar relative to B-pillar is found to be 71.64mm, which is quite close to the limit value of 100.00mm. The performance of this model in controlling the intrusion of A-pillar is average, and it cannot ensure the normal opening function of the door after the collision. According to the solution results, it is necessary to adjust the distance between the A-pillar and the B-pillar, or replace the materials used in the two pillars to improve the material elasticity of the A-pillar and the B-pillar.

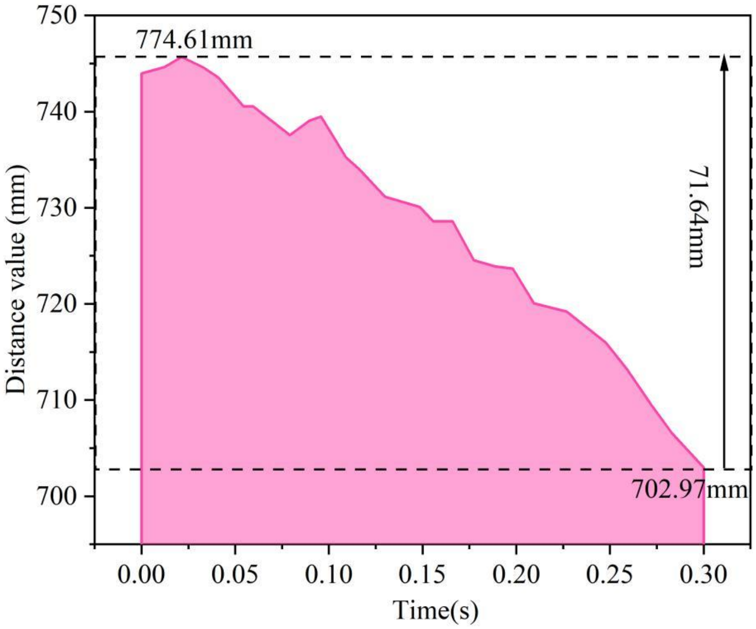

Figure 10: The invasion volume of the A column relative to the B column

4 Conclusion

In this paper, through the high-speed collision simulation test, as well as the Lagrange method nonlinear finite element solution equations, the material structure deformation law of the automobile in extreme conditions is restored and excavated. The displacement of the tail node of the front longitudinal beam reaches 125.66mm, and the downward bending is serious. The deformation of the door frame at two measurement points exceeds the safety requirement of 20mm, and the intrusion of the A-pillar relative to the B-pillar is close to 100.00mm, which is not able to ensure that the occupants can open the door safely to escape after a high-speed collision. Based on the simulation results and the finite element solution results, this paper concludes that the materials used for the front longitudinal beam, A-pillar and B-pillar should be re-selected to improve the robustness of the door frame.

About the Author

Jingtao Wang was born in Qingdao, China, in 1979. He earned a Ph.D. in solid mechanics from Peking University, China in 2007. Since 2015, he has been serving as an associate professor at CAEP Software Center for High Performance Numerical Simulation. His main research interests include novel finite element methods, large-scale engineering simulations and CAE software design.

References

[1] Nanda, T., Singh, V., Singh, G., Singh, M., & Kumar, B. R. (2021). Processing routes, resulting microstructures, and strain rate dependent deformation behaviour of advanced high strength steels for automotive applications. Archives of civil and mechanical engineering, 21(1), 7.

[2] Afolabi, S. O., & Akinsooto, O. (2021). Theoretical framework for dynamic mechanical analysis in material selection for high-performance engineering applications. Noûs, 3, 15-24.

[3] Liu, Y., Ye, H., Yao, Y., & Zhang, L. (2018, July). Research on microstructure and properties of automobile body steel and its development trend. In IOP Conference Series: Materials Science and Engineering (Vol. 382, No. 2, p. 022045). IOP Publishing.

[4] Schmitt, J. H., & Iung, T. (2018). New developments of advanced high-strength steels for automotive applications. Comptes Rendus. Physique, 19(8), 641-656.

[5] Bhandhubanyong, P., & Pearce, J. T. (2018). Materials on Wheels: Moving to Lighter Auto-bodies. International Scientific Journal of Engineering and Technology (ISJET), 2(1), 27-36.

[6] Yang, X., & Zhang, B. (2019). Material embrittlement in high strain-rate loading. International Journal of Extreme Manufacturing, 1(2), 022003.

[7] Wang, F., Yan, H., Zhou, Q., Zhao, S., & Xu, X. (2021). A method of reverse and revision of material mechanics performance parameters for vehicle collision simulation. Thin-Walled Structures, 163, 107681.

[8] Wang, T., Dong, R., Zhang, S., & Qin, D. (2020, November). Research on lightweight design of automobile collision safety structure based on multiple materials. In Journal of Physics: Conference Series (Vol. 1670, No. 1, p. 012004). IOP Publishing.

[9] Atroshenko, S. A., Grigor’ev, A. Y., & Savenkov, G. G. (2019). Mechanisms of plastic deformation in stainless steel under conditions of high-speed penetration of compact strikers. Physics of the Solid State, 61(10), 1690-1694.

[10] Xie, W., Alizadeh-Dehkharghani, A., Chen, Q., Champagne, V. K., Wang, X., Nardi, A. T., ... & Lee, J. H. (2017). Dynamics and extreme plasticity of metallic microparticles in supersonic collisions. Scientific reports, 7(1), 5073.

[11] Shyamsunder, L., Khaled, B., Rajan, S. D., Goldberg, R. K., Carney, K. S., DuBois, P., & Blankenhorn, G. (2020). Implementing deformation, damage, and failure in an orthotropic plastic material model. Journal of Composite Materials, 54(4), 463-484.

[12] Chapuis, A., & Liu, Q. (2018). Effect of strain rate sensitivity in visco-plastic modeling. International Journal of Solids and Structures, 152, 217-227.

[13] Jia, X., Hao, K., Luo, Z., & Fan, Z. (2022). Plastic deformation behavior of metal materials: A review of constitutive models. Metals, 12(12), 2077.

[14] Nelson, A. Z., & Ewoldt, R. H. (2017). Design of yield-stress fluids: A rheology-to-structure inverse problem. Soft matter, 13(41), 7578-7594.

[15] Xu, Z., He, X., Hu, H., Tan, P. J., Liu, Y., & Huang, F. (2019). Plastic behavior and failure mechanism of Ti-6Al-4V under quasi-static and dynamic shear loading. International Journal of Impact Engineering, 130, 281-291.

[16] Smirnov, I. V., Lamzin, D. A., Konstantinov, A. Y., Bragov, A. M., & Lomunov, A. K. (2020). A unified experimental-theoretical approach to predict the critical stress characteristics of failure and yielding under quasi-static and dynamic loading. Engineering Fracture Mechanics, 225, 106197.

[17] Kazemi, S. R. (2020). Plastic deformation due to high-velocity impact using ordinary state-based peridynamic theory. International Journal of Impact Engineering, 137, 103470.

[18] Bragov, A., Igumnov, L., Konstantinov, A., Lomunov, A., & Rusin, E. (2019). Effects of high strain rate and self-heating on plastic deformation of metal materials under fast compression loading. Journal of Dynamic Behavior of Materials, 5(3), 309-319.

[19] Borges, M. F., Neto, D. M., & Antunes, F. V. (2020). Numerical simulation of fatigue crack growth based on accumulated plastic strain. Theoretical and Applied Fracture Mechanics, 108, 102676.

[20] Kocich, R., & Kunčická, L. (2021). Development of structure and properties in bimetallic Al/Cu sandwich composite during cumulative severe plastic deformation. Journal of Sandwich Structures & Materials, 23(8), 4252-4275.

[21] Faraji, G., & Torabzadeh, H. (2019). An overview on the continuous severe plastic deformation methods. Materials transactions, 60(7), 1316-1330.

[22] Liu, Z., Zhang, J., He, Y., & Zhao, W. (2021). A Godunov-type discrete element model for elastic-viscoplastic continuum impact problems. International Journal for Numerical Methods in Engineering, 122(21), 6384-6404.

[23] Zhang, Z., & Liu, D. (2024). A finite-discrete element model for simulating collision and fragmentation of nanoparticle agglomerates. AIChE Journal, 70(1), e18275.

[24] Habtemariam, A. K., Brunnabend, L., Fischer, K., & Stolz, A. (2025). Discrete element method simulation of high-speed vehicle collisions with road barrier systems. Computational Particle Mechanics, 12(1), 709-720.

[25] Nguyen, V. D., Tieu, A. K., André, D., Su, L., & Zhu, H. (2021). Discrete element method using cohesive plastic beam for modeling elasto-plastic deformation of ductile materials. Computational Particle Mechanics, 8(3), 437-457.

[26] Chaussonnet, G., Bravo, L., Flatau, A., Koch, R., & Bauer, H. J. (2020). Smoothed particle hydrodynamics simulation of high velocity impact dynamics of molten sand particles. Energies, 13(19), 5134.

[27] Frissane, H., Taddei, L., Lebaal, N., & Roth, S. (2019). 3D smooth particle hydrodynamics modeling for high velocity penetrating impact using GPU: Application to a blunt projectile penetrating thin steel plates. Computer Methods in Applied Mechanics and Engineering, 357, 112590.

[28] Wang, Y., Li, Q., Xu, Y., Zhou, J., Li, Y., Zhang, D., ... & Jiang, D. (2025). Prediction of hypervelocity impact performance of composite protective structures using a combined finite element method and smoothed particle hydrodynamics approaches. Journal of Mechanical Science and Technology, 39(2), 553-566.

[29] Cerik, B. C. (2017). Large inelastic deformation of aluminium alloy plates in high-speed vessels subjected to slamming. Journal of Marine Science and Technology, 22(2), 301-312.

[30] Xie, S., Yang, W., & Xu, P. (2018). Simulation Analysis of a Multiple-Vehicle, High-Speed Train Collision Using a Simplified Model. Shock and Vibration, 2018(1), 9504141.

[31] Han, L., Jing, L., & Zhao, L. (2018). Finite element analysis of the wheel–rail impact behavior induced by a wheel flat for high-speed trains: The influence of strain rate. Proceedings of the Institution of Mechanical Engineers, Part F: Journal of Rail and Rapid Transit, 232(4), 990-1004.

[32] Zhang, Y., Huang, Y., Liang, K., Cao, K., Wang, Y., Liu, X., ... & Wang, J. (2021). High-precision modeling and collision simulation of small rotor UAV. Aerospace Science and Technology, 118, 106977.

[33] Kota, K. R., Ricks, T., Gomez, L., Monteros, J. E. D. L., Olivares, G., & Lacy Jr, T. E. (2020). Development and validation of finite element impact models of high-density UAS components for use in air-to-air collision simulations. Mechanics of Advanced Materials and Structures, 27(13), 1178-1199.

[34] DeLeon, A., & Palazotto, A. N. (2020). Shock Wave Investigation of High Speed Asperity Collision with Finite Element Modeling. In AIAA Scitech 2020 Forum (p. 0316).

[35] Komine, R., Yasuda, S., Kajihara, M., & Yonezu, A. (2023). Material parameters in constitutive equation for plastic deformation at a high strain rate estimated by high-velocity microparticle collisions. Journal of Materials Engineering and Performance, 32(12), 5627-5637.